Highly ordered square arrays of nanoscale pyramids produced by ion bombardment of a crystalline binary material

Bahaudin Hashmi, Patrick D. Shipman, and R. Mark Bradley

Phys. Rev. E **93**, 032207 — Published 7 March 2016

DOI: 10.1103/PhysRevE.93.032207

Highly Ordered Square Arrays of Nanoscale Pyramids Produced by Ion Bombardment of a Crystalline Binary Material

Bahaudin Hashmi and Patrick D. Shipman

Department of Mathematics, Colorado State University, Fort Collins, CO 80523, USA

R. Mark Bradley

Department of Physics, Colorado State University, Fort Collins, CO 80523, USA

(Dated: December 30, 2015)

Abstract

A theory is developed for the nanoscale patterns formed when the (001) surface of a crystalline binary material with fourfold rotational symmetry is subjected to normal-incidence ion bombardment. The deterministic nonlinear continuum equations account for the Ehrlich-Schwoebel barrier which produces uphill atomic currents on the crystal surface. We demonstrate that highly ordered square arrays of nanopyramids can form in a certain region of parameter space. An Ehrlich-Schwoebel barrier is required for patterns of this kind to develop. For another range of parameters, a disordered square array of nanodots forms, and the pattern coarsens over time.

PACS numbers: 81.16.Rf,79.20.Rf,68.35.Ct,05.45.-a

I. INTRODUCTION

When the planar surface of a binary material is bombarded with a broad ion beam, generally one of the two atomic species is preferentially sputtered, and, as a consequence, a surface layer of altered composition develops. If the solid surface is not flat initially, the spatial variation of the surface height can lead to a surface composition that varies from point to point. This spatially varying surface composition in turn influences the time evolution of the surface topography [1]. The dynamics of the surface morphology and composition are therefore coupled.

This coupling can lead to intriguing types of pattern formation and to a higher degree of order than can be achieved if a surface layer of altered composition is not present. Normal-incidence bombardment of GaSb, for example, can produce an array of nanodots with a remarkable degree of hexagonal order [2–5]. In the case of oblique-incidence bombardment, nearly defect free surface ripples may develop with a spatially oscillating surface composition that mirrors the oscillations of the surface height [6–8]. A "dots-on-ripples" topography in which dots that form a hexagonal array sit atop a ripple topography can also emerge as a result of the coupling [7].

In the models that have been developed so far for these phenomena, it is assumed that the solid is either amorphous or that a surface layer is amorphized by the impinging ions. This assumption is valid, for example, if the target material is a semiconductor that is maintained at a temperature below its recrystallization temperature T_R. However, if the target is a metal single crystal, the crystal structure is not significantly disrupted by the ion bombardment. This is also the case if the target is a crystalline semiconductor held at a temperature T in excess of T_R.

Pattern formation on the surface of elemental materials that remain crystalline during ion bombardment is strongly influenced by the Ehrlich-Schwoebel (ES) barrier [9–12]. The ES barrier produces an uphill atomic current on the crystal's surface and so tends to destabilize an initially flat surface. This current is typically anisotropic, which is a manifestation of the anisotropy of the underlying crystal lattice.

When an Ag (001) surface at a temperature of 200 K was bombarded at normal incidence with a 1 keV Ne^+ beam, a disordered checkerboard pattern of inverted four-sided pyramids was observed [13]. Analogous patterns formed when the (001) surface of germanium was

bombarded at normal incidence and T was maintained at a value not too far in excess of T_R [14]. In both of these experiments, the patterns formed were disordered and there was no surface layer of altered composition. These observations suggest a question: Can highly ordered square arrays of nanoscale pyramids or pyramidal pits be produced by normal-incidence bombardment of the (001) surface of a crystalline binary material?

In this paper, we will study the nanoscale patterns formed when the (001) surface of a crystalline binary material with fourfold rotational symmetry about the z axis is subjected to normal-incidence ion bombardment. We will assume that the material's crystal structure is left intact by the impinging ions; this is a reasonable assumption if the material is a substitutional alloy of two metals or if it is a binary semiconductor that is held at a temperature above T_R. As we will demonstrate, for certain ranges of the parameters, highly ordered square arrays of four-sided pyramids emerge. An Ehrlich-Schwoebel barrier is essential if patterns of this kind are to form — diffusional anisotropy alone does not yield orderly square arrays.

This paper is organized as follows: We develop the equations of motion in Section II. In Section III, we find the domain in parameter space in which there is a narrow band of unstable wavelengths. It is in this region of parameter space that a Turing instability that leads to a well-ordered pattern may occur. In Section IV, we derive the amplitude equations which describe the pattern formation that occurs near the Turing instability. Stability analysis of the steady-state solutions to the amplitude equations gives rise to conditions for the formation of ripple or square patterns. In Section V, we carry out numerical simulations of the original equations of motion developed in Section II and compare the results with the amplitude equation analysis. Physical implications of our results and a summary of our conclusions are given in Section VI.

II. EQUATIONS OF MOTION

In groundbreaking work, Shenoy, Chan and Chason studied the coupling between the surface topography and composition that arises during ion bombardment of a binary compound [1]. Bradley and Shipman (BS) extended this theory to include the effect of mass redistribution and the leading order nonlinear terms [3–5]. The BS equations govern the behavior of $u(x, y, t)$ and $\phi(x, y, t)$, the deviations of the surface height and surface concen-

tration from their unperturbed, steady-state values. Using the same notation, assumptions and rescaling as BS employed, we have

$$\frac{\partial u}{\partial t} = \phi - \nabla^2 u - \nabla^2 \nabla^2 u + \lambda (\nabla u)^2 \tag{1}$$

and

$$\frac{\partial \phi}{\partial t} = -a\phi + b\nabla^2 u + c\nabla^2 \phi + \nu \phi^2 + \eta \phi^3 \tag{2}$$

for normal-incidence bombardment. Explicit expressions that relate the dimensionless constants a, b, c, λ, ν and η to the underlying physical parameters may be found in Ref. [4].

It is assumed that the binary solid is either amorphous or that the incident ions amorphize a layer at the surface of the solid in the BS theory. The surface mass currents included in the theory result from surface diffusion and ion-induced mass redistribution.

In this paper, we will study the time evolution of the (001) surface of a crystalline binary solid that is bombarded with a broad ion beam at normal incidence. We assume that the crystal structure of the solid has fourfold rotational symmetry about the z axis. Examples of binary compound semiconductors having this property are the IV-VI materials PbSe, PbS, PbTe and SnTe, all of which have the halite crystal structure.

When the semiconducting compounds GaAs and InAs are subjected to normal-incidence bombardment at temperatures in excess of T_R, nearly defect free surface ripples result [15]. These materials have a zincblende crystal structure. As a result, they only have twofold rotational symmetry about the z axis. The theory developed here therefore does not apply to these experiments.

Although the incident ions introduce defects into the crystal lattice, it will be assumed that these are rapidly annealed away so that the solid remains a nearly defect-free crystal during the bombardment. In this case, the ES surface atomic currents must be added to the currents that stem from surface diffusion and mass redistribution. The surface currents of the two atomic species A and B that are produced by the ES barrier may be written [10, 12]

$$\boldsymbol{J}_i^{(\mathrm{ES})} = e_i \begin{pmatrix} u_x(1 - p_i u_x^2 - q_i u_y^2) \\ u_y(1 - q_i u_x^2 - p_i u_y^2) \end{pmatrix}. \tag{3}$$

Here $i = A$, B, the subscripts on u denote partial derivatives and e_A, e_B, p_A, p_B, q_A and q_B are constants that depend on the choice of target material and ion beam. In addition, surface diffusion is in general anisotropic on the crystal surface. In the BS theory, the surface

currents produced by surface diffusion and capillarity are isotropic and may be written

$$\boldsymbol{J}_i^{(\mathrm{SD})} = D_i \boldsymbol{\nabla} \nabla^2 u, \tag{4}$$

where $i = A$, B and the positive constants D_A and D_B are proportional to the diffusivities of the two atomic species. These currents take the form

$$\boldsymbol{J}_i^{(\mathrm{SD})} = D_i \boldsymbol{\nabla} \nabla^2 u + C_i (u_{xyy} \hat{\boldsymbol{x}} + u_{xxy} \hat{\boldsymbol{y}}) \tag{5}$$

for the problem at hand. The magnitudes of the constants C_A and C_B gauge the extent to which the surface diffusion is anisotropic on the crystal's surface. In the BS theory, $e_A = e_B = C_A = C_B = 0$.

We now adopt the same assumptions and approximations as BS employed, except that it will be assumed that the solid remains crystalline during the ion bombardment, as we already stated. The analysis very closely parallels the detailed derivation in Ref. [4] and so we will only give the resulting rescaled equations of motion. They are

$$u_t = \phi - \nabla^2 u - \nabla^2 \nabla^2 u + \lambda (\nabla u)^2 + \rho u_{xxyy} + \partial_x [u_x (\alpha_1 u_x^2 + \beta_1 u_y^2)] + \partial_y [u_y (\beta_1 u_x^2 + \alpha_1 u_y^2)] \tag{6}$$

and

$$\phi_t = -a\phi + b\nabla^2 u + c\nabla^2 \phi + \nu \phi^2 + \eta \phi^3 + \partial_x [u_x (\alpha_2 u_x^2 + \beta_2 u_y^2)] + \partial_y [u_y (\beta_2 u_x^2 + \alpha_2 u_y^2)]. \tag{7}$$

The explicit expressions that relate the dimensionless parameters a, b, c, λ, ν, η, ρ, α_1, α_2, β_1 and β_2 to the underlying physical parameters are readily obtained. They are, however, quite lengthy and not particularly illuminating and so we will not pause to list them here. If there is no ES barrier, then $\alpha_1 = \alpha_2 = \beta_1 = \beta_2 = 0$ and if, in addition, diffusion is isotropic, then $\rho = 0$. In that event, the BS equations (1) and (2) are recovered.

If the term ϕ is dropped from Eq. (6), the surface morphology is not coupled to the composition. The resulting equation is similar to the equation of motion used by Ou *et al.* to model normal-incidence bombardment of the (001) surface of a germanium sample held at a temperature above its recrystallization temperature [14]. In the model employed by Ou *et al.*, however, $\rho = \lambda = \beta_1 = 0$. This means that they assumed the surface diffusion to be isotropic, neglected the nonlinearity coming from sputtering, and adopted a particular form for the ES terms. These simplifications seem to be good approximations for their experiments. Ou *et al.* also included the conserved Kuramoto-Sivashinsky nonlinearity

$\nabla^2(\nabla u)^2$ in their equation of motion. This leads the surface patterns to coarsen with time, in accord with their experiments.

In our model, it is sufficient to consider only values of the parameter ρ that are less than or equal to zero. To see this, we choose a new coordinate system that is obtained by rotating the original coordinate system by 45° and then rescaling [16]. Explicitly, we set $\tilde{x} = (2r)^{-1/2}(x+y)$, $\tilde{y} = (2r)^{-1/2}(-x+y)$, $\tilde{t} = r^{-1}t$, $\tilde{u} = u$ and $\tilde{\phi} = r\phi$, where $r \equiv 1 - \rho/4$. This yields

$$\tilde{u}_{\tilde{t}} = \tilde{\phi} - \tilde{\nabla}^2\tilde{u} - \tilde{\nabla}^2\tilde{\nabla}^2\tilde{u} + \tilde{\lambda}(\tilde{\nabla}u)^2 + \tilde{\rho}\tilde{u}_{\tilde{x}\tilde{x}\tilde{y}\tilde{y}} + \partial_{\tilde{x}}[\tilde{u}_{\tilde{x}}(\tilde{\alpha}_1\tilde{u}_{\tilde{x}}^2 + \tilde{\beta}_1\tilde{u}_{\tilde{y}}^2)] + \partial_{\tilde{y}}[\tilde{u}_{\tilde{y}}(\tilde{\beta}_1\tilde{u}_{\tilde{x}}^2 + \tilde{\alpha}_1\tilde{u}_{\tilde{y}}^2)] \quad (8)$$

and

$$\tilde{\phi}_{\tilde{t}} = -\tilde{a}\tilde{\phi} + \tilde{b}\tilde{\nabla}^2\tilde{u} + \tilde{c}\tilde{\nabla}^2\tilde{\phi} + \tilde{\nu}\tilde{\phi}^2 + \tilde{\eta}\tilde{\phi}^3 + \partial_{\tilde{x}}[\tilde{u}_{\tilde{x}}(\tilde{\alpha}_2\tilde{u}_{\tilde{x}}^2 + \tilde{\beta}_2\tilde{u}_{\tilde{y}}^2)] + \partial_{\tilde{y}}[\tilde{u}_{\tilde{y}}(\tilde{\beta}_2\tilde{u}_{\tilde{x}}^2 + \tilde{\alpha}_2\tilde{u}_{\tilde{y}}^2)]. \quad (9)$$

Here $\tilde{a} = ra$, $\tilde{b} = rb$, $\tilde{c} = c$, $\tilde{\lambda} = \lambda$, $\tilde{\nu} = \nu$, $\tilde{\eta} = r^{-1}\eta$,

$$\tilde{\rho} = -\frac{\rho}{1-\rho/4}, \quad (10)$$

$$\tilde{\alpha}_1 = \frac{1}{4r}(\alpha_1 + \beta_1), \quad (11)$$

$$\tilde{\beta}_1 = \frac{1}{4r}(3\alpha_1 - \beta_1), \quad (12)$$

$$\tilde{\alpha}_2 = \frac{1}{4}(\alpha_2 + \beta_2), \quad (13)$$

and

$$\tilde{\beta}_2 = \frac{1}{4}(3\alpha_2 - \beta_2). \quad (14)$$

If we were to drop the tildes, Eqs. (8) and (9) would be identical to Eqs. (6) and (7). We shall see in the next section that for the theory to be well posed, ρ must be less than 4. Thus, if ρ is positive, Eq. (10) shows that we may adopt a rotated and rescaled coordinate system in which $\tilde{\rho}$ (the transformed value of ρ) is negative. We will therefore confine our attention to $\rho \leq 0$ in what follows.

III. LINEAR STABILITY ANALYSIS

We now determine whether or not the flat, compositionally homogeneous steady-state solution $u = \phi = 0$ is linearly stable for a given set of parameter values. Consider a

perturbation to the steady state that is small enough that the nonlinear terms may be dropped from Eqs. (6) and (7), yielding the linearized equations of motion. We seek solutions to these equations of the form

$$\begin{pmatrix} u \\ \phi \end{pmatrix} = \begin{pmatrix} u_* \\ \phi_* \end{pmatrix} \exp(i\boldsymbol{k}\cdot\boldsymbol{x} + \sigma t), \tag{15}$$

where $\boldsymbol{k} \equiv k_x\hat{x} + k_y\hat{y}$, $\boldsymbol{x} \equiv x\hat{x} + y\hat{y}$ and u_* and ϕ_* are constants. $\mathrm{Re}\,\sigma$ gives the rate with which the amplitude of the mode grows (for $\mathrm{Re}\,\sigma > 0$) or attenuates (for $\mathrm{Re}\,\sigma < 0$). For each wavevector $\boldsymbol{k}$, there are two possible values of σ, given by

$$2\sigma_\pm = f \pm \sqrt{g}, \tag{16}$$

where $k \equiv |\boldsymbol{k}|$,

$$f(k, a, c, \alpha) \equiv -a + (1-c)k^2 - k^4 + \rho k_x^2 k_y^2 \tag{17}$$

and

$$g(k, a, b, c, \alpha) \equiv \left[a + (1+c)k^2 - k^4 + \rho k_x^2 k_y^2\right]^2 - 4bk^2. \tag{18}$$

We will assume that $\rho < 4$ since in that case $\mathrm{Re}\,\sigma_+$ and $\mathrm{Re}\,\sigma_-$ are both negative for sufficiently large wavenumbers k, and the theory is therefore well posed.

The remainder of the linear stability analysis closely parallels that given elsewhere [4] for the special case $\rho = 0$ and so only the results will be given. For fixed $\rho \leq 0$, we partition the positive quadrant of the (a, c) plane into three regions (see Figure 1 of Ref. [4]):

In Region I, $c > a$ and $4a > (1-c)^2$ if $c < 1$;

In Region II, $c < a$ and $4a > (1-c)^2$ if $c < 1$;

In Region III, $c < 1$ and $4a < (1-c)^2$.

The necessary and sufficient condition for the solid surface to be unstable in Region I is $b < b_T$, where

$$b_T \equiv \frac{(c+a)^2}{4c}. \tag{19}$$

The surface is unstable in Region II if $b < a$. Finally, in Region III, the surface is unstable for arbitrary values of b.

For the weakly nonlinear analysis that follows, we will confine our attention to Region I since it is for parameter values in this region that stable well-ordered patterns can form.

Consider the case $b = b_T$. If $\rho < 0$ and the point (a, c) lies in Region I, then σ_+ is zero for $\boldsymbol{k} = 0$ and $\pm\boldsymbol{k}_1$ and $\pm\boldsymbol{k}_2$, where $\boldsymbol{k}_1 \equiv k_T\hat{x}$, $\boldsymbol{k}_2 \equiv k_T\hat{y}$ and k_T is given by

$$k_T^2 = \frac{c-a}{2c}. \tag{20}$$

If $\rho = 0$, on the other hand, then σ_+ is zero for $\boldsymbol{k} = 0$ and $\boldsymbol{k}$ such that $|\boldsymbol{k}| = k_T$. The real part of $\sigma_+(\boldsymbol{k})$ is negative for all other $\boldsymbol{k}$ for both $\rho = 0$ and $\rho < 0$. A Turing instability therefore occurs for $b = b_T$ [17–19]. For b just below b_T, there is a narrow annular region in $\boldsymbol{k}$ space in which $\mathrm{Re}\,\sigma_+(\boldsymbol{k}) > 0$ for the case $\rho = 0$, whereas for $\rho < 0$, there are small regions in $\boldsymbol{k}$ space about each of the points $\pm\boldsymbol{k}_1$ and $\pm\boldsymbol{k}_2$ in which $\mathrm{Re}\,\sigma_+(\boldsymbol{k})$ is positive. These regions are shown in Fig. 1.

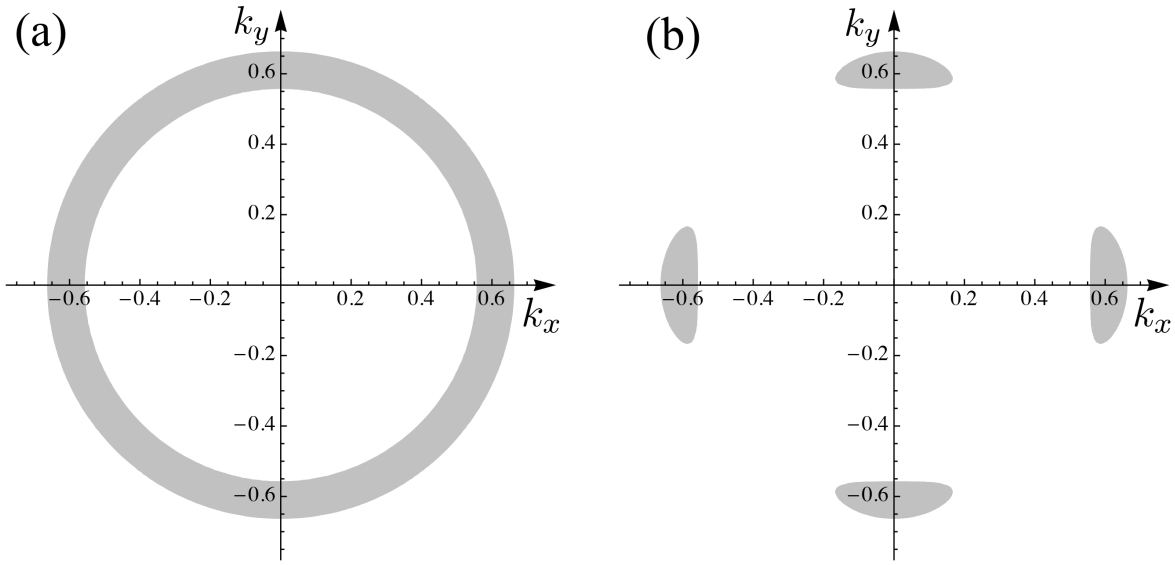

FIG. 1: Regions in wavevector space in which $\mathrm{Re}\,\sigma_+(\boldsymbol{k}) > 0$ for $a = 0.25$ and $c = 1$ (shaded). In (a) $\rho = 0$ and $b = 0.99b_T \simeq 0.3867$, while in (b) $\rho = -0.25$ and $b = 0.99b_T \simeq 0.3867$.

IV. WEAKLY NONLINEAR ANALYSIS

We now analyze Eqs. (6) and (7) close to the Turing transition. We assume that the values of the parameters a and c lie in Region I so that $c > a$ and $4a > (1-c)^2$ if $c < 1$. The bifurcation parameter b is taken to be slightly below the critical value b_T: we set $b = b_T - \epsilon$, where $\epsilon > 0$ is small and positive. As discussed in Sec. III, if $\rho < 0$ and b is close enough

to b_T, then there are small regions about the wavevectors $\pm\boldsymbol{k}_1$ and $\pm\boldsymbol{k}_2$ in which $\mathrm{Re}\,\sigma_+(\boldsymbol{k})$, is positive; if $\rho = 0$, there is an annular region of such modes. The analysis, which yields ordinary differential equations for the time-evolution of the amplitudes of these unstable modes [17–19], is similar to that we have given elsewhere [3, 4] for normal-incidence ion bombardment of binary materials and so only the principal results will be given here.

We obtain approximate solutions to the equations of motion of the form

$$\begin{pmatrix} u \\ \phi \end{pmatrix} = \sum_{j=1}^{2} \begin{pmatrix} 1 \\ \frac{a^2-c^2}{4c^2} \end{pmatrix} (A_j \mathrm{e}^{i\boldsymbol{k}_j\cdot\boldsymbol{x}} + \text{c.c.}) + \begin{pmatrix} G \\ 0 \end{pmatrix}, \tag{21}$$

where the complex-valued amplitudes A_j and real-valued amplitude G vary slowly with time and c.c. denotes the complex conjugate. The Goldstone mode with $u = G$ and $\phi = 0$ corresponds to the neutrally stable wavenumber $k = 0$; physically, this mode is simply a vertical displacement of the surface. Although this mode is not linearly unstable, it may not be neglected, due to its interactions with the linearly unstable modes through the nonlinear terms in the equations of motion. In the case $\rho < 0$, the vectors $\boldsymbol{k}_j$ in the sum in Eq. (21) are $\boldsymbol{k}_1 = k_T\hat{x}$ and $\boldsymbol{k}_2 = k_T\hat{y}$ since the corresponding Fourier modes have the largest growth rates. In the case in which ρ vanishes, $\boldsymbol{k}_1$ and $\boldsymbol{k}_2$ could be any pair of vectors with length k_T.

The solvability conditions obtained by expanding Eqs. (6) and (7) to second order in ϵ yield equations that govern the time dependence of the amplitudes A_1, A_2 and G. We find that

$$\frac{dA_1}{dt} = \sigma A_1 - \gamma A_1(\gamma_1|A_1|^2 + \gamma_2|A_2|^2), \tag{22}$$

$$\frac{dA_2}{dt} = \sigma A_2 - \gamma A_2(\gamma_2|A_1|^2 + \gamma_1|A_2|^2), \tag{23}$$

where

$$\sigma \equiv \frac{2c(c-a)}{(c+a)(2c^2+a-c)}(b_T - b)\,, \tag{24}$$

$$\gamma \equiv \frac{2c^2}{2c^2+a-c}, \tag{25}$$

and in the case $\rho < 0$,

$$\gamma_1 \equiv \frac{3\eta(c-a)^3(a+c)^2}{32c^6} + 3(a\alpha_1 + c\alpha_1 + 2\alpha_2), \tag{26}$$

and

$$\gamma_2 \equiv \frac{6\eta(c-a)^3(a+c)^2}{32c^6} + 4(a\beta_1 + c\beta_1 + 2\beta_2). \tag{27}$$

If $\rho = 0$, the coefficients of the cubic terms in Eqs. (22) and (23) are functions of the wavevectors $\boldsymbol{k}_1$ and $\boldsymbol{k}_2$. Setting $c_j = \cos(\theta_j)$, $s_j = \sin(\theta_j)$, and $\boldsymbol{k}_j = k_T(c_j, s_j)$ for $j = 1$ and 2, the coefficients γ_1 and γ_2 become

$$\gamma_1 \equiv \frac{3\eta(c-a)^3(a+c)^2}{32c^6} + 3(a\alpha_1 + c\alpha_1 + 2\alpha_2)(c_1^4 + s_1^4) + 6(a\beta_1 + c\beta_1 + 2\beta_2)c_1^2 s_1^2, \qquad (28)$$

and

$$\gamma_2 \equiv \frac{6\eta(c-a)^3(a+c)^2}{32c^6} + 6(a\alpha_1 + c\alpha_1 + 2\alpha_2)(c_1^2 c_2^2 + s_1^2 s_2^2) + 4(a\beta_1 + c\beta_1 + 2\beta_2)(c_1^2 s_2^2 + c_1 s_1 c_2 s_2 + s_1^2 c_2^2). \qquad (29)$$

We also obtain

$$\frac{dG}{dt} = \left[\lambda\left(1 - \frac{a}{c}\right) + \frac{2\nu}{a}\left(\frac{c^2 - a^2}{4c^2}\right)^2\right](|A_1|^2 + |A_2|^2) \qquad (30)$$

for any value of ρ. The value of dG/dt gives the change in the net sputter yield that stems from the spatial variations in the surface height and composition. As shown by Eq. (30), dG/dt may be either positive or negative, depending on the values of the coefficients. Thus, the Goldstone mode either increases the spatially-averaged sputter yield (if $dG/dt < 0$) or reduces it (if $dG/dt > 0$). The real amplitude G does not appear on the right-hand side of either Eqs. (22), (23) or (30) since only derivatives of u appear in the equations of motion, and we are assuming that G does not vary in space.

A detailed analysis of the amplitude equations (22) and (23) may be found in Ref. [17]; here we summarize the results. The system of equations (22) and (23) admits stationary solutions of three different types that are stable for some range of σ:

1. *Homogeneous state:* $A_1 = A_2 = 0$. This solution is the undisturbed steady state $u = \phi = 0$ and is stable for $\sigma < 0$ (equivalently, for $b > b_T$).

2. *Roll pattern:* $A_1 = (\sigma/\gamma\gamma_1)^{1/2} e^{ip}$ and $A_2 = 0$, or $A_1 = 0$ and $A_2 = (\sigma/\gamma\gamma_1)^{1/2} e^{ip}$. Here p is an arbitrary phase. These solutions are surface ripples (or "rolls") with wavevectors $\boldsymbol{k}_1$ and $\boldsymbol{k}_2$ and are stable for $\sigma > 0$ and $\gamma_1 < |\gamma_2|$.

3. *Square pattern:* $A_1^2 = \frac{\sigma}{\gamma(\gamma_1+\gamma_2)} e^{ip_1}$ and $A_2^2 = \frac{\sigma}{\gamma(\gamma_1+\gamma_2)} e^{ip_2}$, where p_1 and p_2 are arbitrary phases. These solutions are square arrays of nanodots or nanoholes and are stable for $\sigma > 0$ and $\gamma_1 > |\gamma_2|$.

If b is slightly less than b_T, then σ is positive and the flat steady-state solution is unstable. If $\rho < 0$ and $\gamma_1 < |\gamma_2|$, then partially intersecting patches of surface ripples with wavevectors $\boldsymbol{k}_1$ and $\boldsymbol{k}_2$ begin to form as the instability sets in. If, as in our idealized model, there is no source of noise, ultimately only one ripple orientation will survive and the fourfold rotational symmetry about the z axis will be broken. In an experiment, however, there is shot noise in the ion beam and one ripple orientation will never cover the entire sample.

For $\rho < 0$ and $\sigma > 0$, the condition $\gamma_1 > |\gamma_2|$ that must be satisfied for square solutions to be stable may be written

$$3(a+c)\alpha_1 + 6\alpha_2 > 3\xi(a+c) + 4(a+c)\beta_1 + 8\beta_2 \quad \text{if} \quad \gamma_2 > 0, \quad \text{or}$$

$$3(a+c)\alpha_1 + 6\alpha_2 > -9\xi(a+c) - 4(a+c)\beta_1 - 8\beta_2 \quad \text{if} \quad \gamma_2 < 0, \tag{31}$$

where $\xi \equiv \eta(c-a)^3(a+c)/(32c^6)$ is positive for a and c in Region I. For the simpler case in which $\alpha_2 = \beta_2 = 0$, this condition reduces to

$$\alpha_1 > \frac{4}{3}\beta_1 + \xi \quad \text{if} \quad \beta_1 > -\frac{2}{3}\xi, \quad \text{or}$$

$$\alpha_1 > -\frac{4}{3}\beta_1 - 3\xi \quad \text{if} \quad \beta_1 < -\frac{2}{3}\xi.$$

The region in the (α_1, β_1) plane for which square solutions are stable if $\alpha_2 = \beta_2 = 0$ is shown as the shaded region in Fig. 2. This region is bounded away from the origin in the (α_1, β_1) plane. In particular, if there is no Ehrlich-Schwoebel barrier (so that $\alpha_1 = \alpha_2 = \beta_1 = \beta_2 = 0$), a square array of nanodots or nanoholes is not stable. This means that diffusional anisotropy alone is not sufficient to stabilize a square pattern — an ES barrier is needed as well. Moreover, not just any ES terms will do — the ES coefficients must satisfy the condition (31) if a square pattern is to form.

Because $c > a$ in Region I, Eq. (21) shows that the spatial variations of u and ϕ are 180° out of phase. As a consequence, the preferentially sputtered species is most concentrated at the highest points of the surface.

The situation is completely analogous for $0 < \rho < 4$. The only difference between this case and the case $\rho < 0$ is that the two possible ripple wavevectors are $\boldsymbol{k}_3$ and $\boldsymbol{k}_4$, where $\boldsymbol{k}_3 \equiv k_T(\hat{x} + \hat{y})/\sqrt{2}$ and $\boldsymbol{k}_4 \equiv k_T(\hat{x} - \hat{y})/\sqrt{2}$ and k_T is given by

$$k_T^2 = \frac{c - (1+\alpha)a}{2c(1+\alpha)}. \tag{32}$$

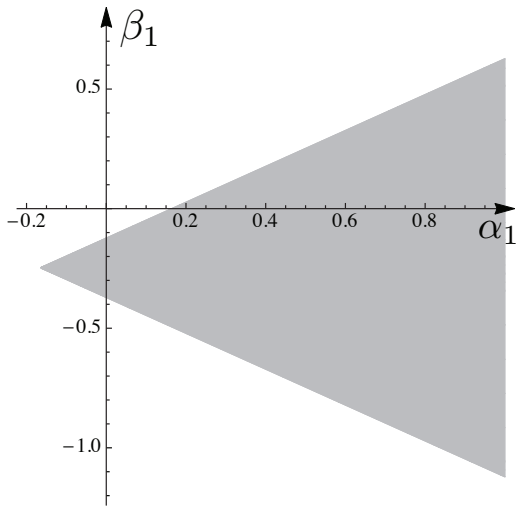

FIG. 2: The region in the (α_1, β_1) plane for which $\gamma_1 > |\gamma_2|$ if $\alpha_2 = \beta_2 = 0$ is shaded. The other parameters are $a = 0.25$, $c = 1$, and $\eta = 10$. Square patterns are stable for (α_1, β_1) in this region if $\sigma > 0$.

As a consequence, the ripples form 45° angles with the $x-$ and $y-$axes when $\rho > 0$.

For the case $\rho = 0$, the linear stability analysis yields an entire annulus of wavevectors corresponding to unstable modes and therefore does not put any restriction on the angles θ_j. In fact, the wavevectors chosen by the dynamics may not even be orthogonal to each other. A prediction of the chosen angles θ_1 and θ_2 may be obtained by realizing that, although the system of partial differential equations (PDEs) given by Eqs. (8) and (9) is not a gradient system, the system of amplitude equations given by Eqs. (22) and (23) is. Indeed, defining the effective potential

$$P(A_1, A_1^*, A_2, A_2^*; \theta_1, \theta_2, \boldsymbol{p}) \equiv -\sigma(A_1 A_1^* + A_2 A_2^*) + \frac{1}{2}\gamma \left[\gamma_1 A_1^2 (A_1^*)^2 + 2\gamma_2 A_1 A_1^* A_2 A_2^* + \gamma_1 A_2^2 (A_2^*)^2\right], \tag{33}$$

where $\boldsymbol{p}$ is the vector of parameters, the amplitude equations may be written as

$$\frac{dA_j}{dt} = -\frac{\partial}{\partial A_j^*} P$$

for $j = 1, 2$. This implies that the effective potential P decreases with time until a local minimum is reached and the pattern stops evolving.

For a given choice of the angles θ_j, the system of amplitude equations may be solved for the stationary pattern $A_1^2 = A_2^2 = \frac{\sigma}{\gamma(\gamma_1 + \gamma_2)} e^{ip}$, and the corresponding effective potential may

be found. For a given set of parameters, the effective potential thus becomes a function of the angles θ_j, and we can determine what choice of angles minimizes the effective potential. We return to an analysis of the potential landscape in Section V, where we predict the angles θ_j by finding the minima of the effective potential and compare the prediction to the results of a simulation with $\rho = 0$ (see Fig. 7). A similar approach has been successfully applied in other contexts [20, 21] in which the system of PDEs is not a gradient system but the system of amplitude equations derived from the PDEs near the onset of a pattern is.

V. NUMERICAL SIMULATIONS

In this section, we compare our analytical results with numerical simulations of the original system of partial differential equations, Eqs. (6) and (7). For all simulations, the initial conditions are low-amplitude white noise. We employ a Fourier spectral method with periodic boundary conditions and a fourth-order exponential time differencing Runge-Kutta method for the time stepping as the numerical technique [22, 23]. The spatial grid is 256×256 unless otherwise noted.

As predicted by the amplitude equation analysis, for $\rho < 0$ and b slightly less than b_T, a pattern with stripes parallel to either the x- or y-axis forms for $\gamma_1 < |\gamma_2|$ (Fig. 3 (a)), whereas a square pattern aligned with the x- and y-axes forms for $\gamma_1 > |\gamma_2|$ (Fig. 3 (c)). Figs. 3 (b) and (d) show a histograms of the surface gradients $\nabla u = (u_x, u_y)$ for the patterns shown in Figs. 3 (a) and (c) respectively. In both cases, the histogram has strong peaks. In the case of the square pattern, the peaks are at the four corners of a square, indicating that the pattern is composed of faceted pyramids with nearly flat faces. The ripples are faceted as well since there are two peaks on the u_y axis that are equidistant from the origin.

In Fig. 4, we show the time-evolution of the pattern for the particular case $\alpha_2 = \beta_2 = 0$ discussed in Section IV. For the chosen parameters, $\beta_1 > -\frac{2}{3}\xi$, and, as predicted by the analysis, the steady-state pattern consists of ripples if $\alpha_1 < \frac{4}{3}\beta_1 + \xi$ (so that $\gamma_1 < |\gamma_2|$), as in Fig. 4 (c), whereas the steady state pattern consists of squares if $\alpha_1 > \frac{4}{3}\beta_1 + \xi$ (so that $\gamma_1 > |\gamma_2|$), as in Fig. 4 (f). Note that in Figs. 4 (a)-(c) the pattern evolves to ripples through states in which there are patches of squares.

The simulations shown in Fig. 5 show that even if $\rho \neq 0$, terms arising from the Ehrlich-Schwoebel barrier are necessary if a well-ordered pattern of squares is to form. If there is

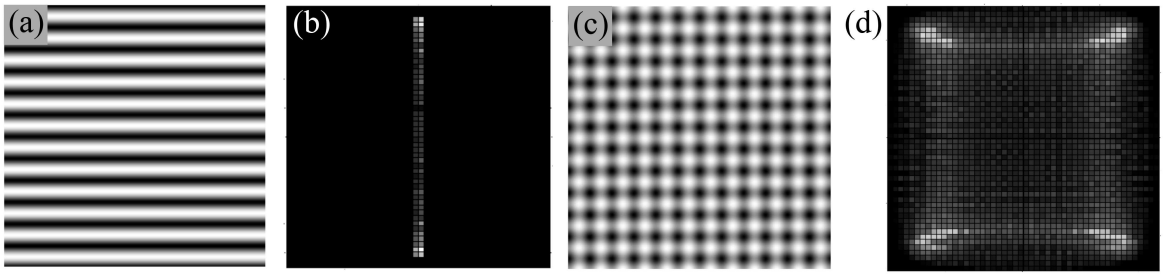

FIG. 3: (a) and (c): Gray-scale plots of $u(x, y, t)$ at time $t = 20000$ resulting from numerical simulations of Eqs. (6) and (7) for $a = 0.25$ and $c = 1$ in Region I. For both simulations, $\rho = -0.25$, $\lambda = -1$, $\nu = 1$, and $\eta = 10$. For panel (a), $\alpha_1 = 0.5$, $\alpha_2 = 0.5$, $\beta_1 = 1$, and $\beta_2 = 1$, whereas for panel (c), $\alpha_1 = 0.5$, $\alpha_2 = 0.5$, $\beta_1 = 0.25$, and $\beta_2 = 0.25$. For both plots, the domain is $-60 \leq x, y \leq 60$. For these parameter values, $\gamma_1 = 5.493$. In addition, $\gamma_2 = 14.236$ for panel (a), whereas $\gamma_2 = 4.486$ for panel (c). (b) and (d): Histograms of (u_x, u_y) for the surfaces in panel (a) and (c) respectively. The domain is $-0.9 \leq u_x, u_y \leq 0.9$ for (b) and $-0.8 \leq u_x, u_y \leq 0.8$ for (d).

no ES barrier (so that $\alpha_1 = \alpha_2 = \beta_1 = \beta_2 = 0$), a pattern of rolls forms if the coefficients λ and ν of the quadratic terms in the equations of motion are zero (Fig. 5 (a)). As illustrated in Fig. 5 (b,c), the effect of nonzero quadratic coefficients is to produce a pattern which has more resemblance to squares for b closer to the critical value b_T ($b = 0.99b_T$ for Fig. 5 (b), whereas $b = 0.96b_T$ for Fig. 5 (c)). In both cases, however, the patterns display little order.

The simulations shown in Fig. 6 further illustrate the impact of quadratic nonlinearities on the pattern. The coefficients in the amplitude equations (22) and (23) do not depend on the coefficients λ and ν of the quadratic terms in the equations of motion. In the case in which $\rho = 0$ and there is no Ehrlich-Schwoebel barrier (so that $\alpha_1 = \beta_1 = \alpha_2 = \beta_2 = 0$), our results in Refs. [3] and [4] predict hexagonal patterns in Region I for large enough magnitudes of λ or ν. In the simulations pictured in Fig. 6, we select parameters that would give a hexagonal pattern, except that we choose $\rho < 0$, fix $\beta_1 = \beta_2 = 0.25$ and vary $\alpha_1 = \alpha_2$. Our amplitude equation analysis predicts a square pattern for large enough $\alpha_1 = \alpha_2$, and our simulations confirm this prediction. However, the pattern is only well ordered for large enough $\alpha_1 = \alpha_2$. This provides additional evidence that Ehrlich-Schwoebel coefficients of sufficient magnitude are essential for the formation of well-ordered square patterns.

As discussed in Sec. III, for $\rho = 0$, it is not apparent from linear stability analysis that the pattern will be aligned with the x or y axes or that the chosen wavevectors $\boldsymbol{k}_1 =$

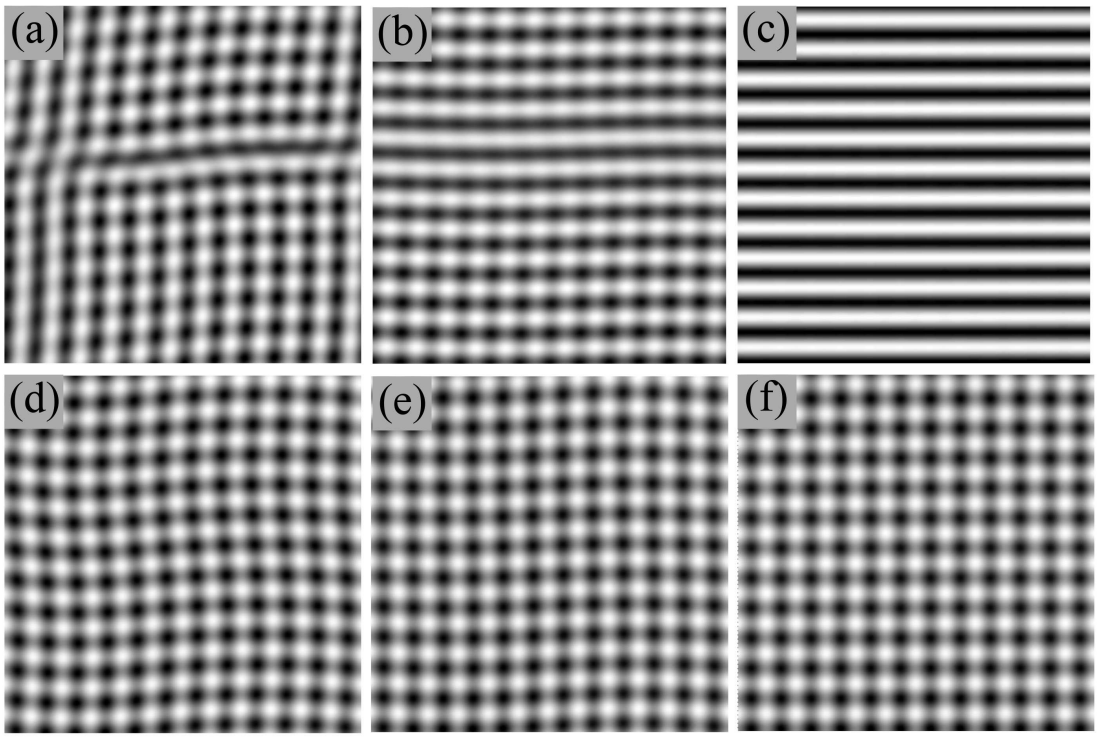

FIG. 4: Gray-scale plots of $u(x, y, t)$ resulting from two numerical simulations of Eqs. (6) and (7). Each row is a time series of a simulation. For each simulation, $a = 0.25$, $c = 1$, $\rho = -0.25$, $\lambda = 0$, $\nu = 0$, and $\eta = 10$. For the top row, $\alpha_1 = 0.25$, $\alpha_2 = 0$, $\beta_1 = 0.25$, and $\beta_2 = 0$, whereas for the bottom row, $\alpha_1 = 0.6$, $\alpha_2 = 0$, $\beta_1 = 0.25$, and $\beta_2 = 0$. For these parameter values, $\gamma_2 = 2.486$. In addition, $\gamma_1 = 1.555$ for the top row, whereas $\gamma_1 = 2.868$ for the bottom row. For all plots, the domain is $-60 \leq x, y \leq 60$. The times are (a) 2000, (b) 5000, (c) 10000 for the simulation of the top row, and (d) 2000, (e) 3000, (f) 10000 for the simulation of the bottom row.

$(\cos(\theta_1), \sin(\theta_1))$ and $\boldsymbol{k}_2 = (\cos(\theta_2), \sin(\theta_2))$ will be orthogonal. In Fig. 7 (d), we plot the effective potential (33) as a function of θ_1 and θ_2. The effective potential has minima at $(\theta_1, \theta_2) = (\pi/2, 0)$ and $(0, \pi/2)$ and at equivalent choices of (θ_1, θ_2) that correspond to a square pattern aligned with the coordinate axes. In accordance with this prediction, in the time series shown in Fig. 7 (a)-(c) for $\rho = 0$ and $\gamma_1 > |\gamma_2|$, the system system evolves to a pattern of patches of squares that are aligned with the coordinate axes.

Our weakly nonlinear analysis and resulting amplitude equations are not applicable for parameter values a and c in Region II. We explore this regime with numerical simulations, as given in Figs. 8 and 9 for $\rho < 0$ and in Fig. 10 for $\rho = 0$. If $\rho < 0$, the pattern coarsens

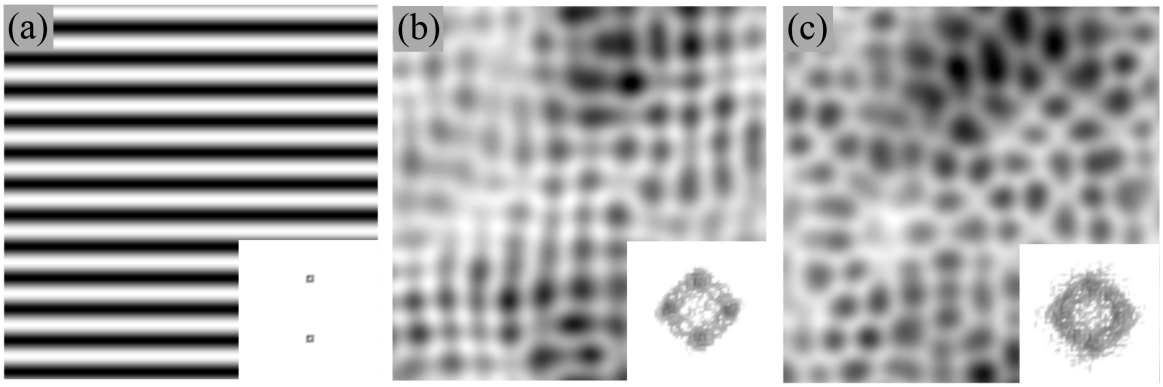

FIG. 5: Gray-scale plots of $u(x, y, t)$ resulting from numerical simulations of Eqs. (6) and (7). For each simulation, $a = 0.25$, $c = 1$, $\rho = -0.25$, $\nu = 0$, and $\eta = 10$, $\alpha_1 = \alpha_2 = \beta_1 = \beta_2 = 0$, and the time is $t = 30,000$. For panels (a) and (b), $b = 0.99b_T$, whereas for panel (c), $b = 0.96b_T$. For panel (a), $\lambda = 0$, whereas for panels (b) and (c), $\lambda = -0.5$. For all plots, the domain is $-60 \leq x, y \leq 60$. Insets show the Fourier transform on the domain $-12 \leq k_x, k_y \leq 12$.

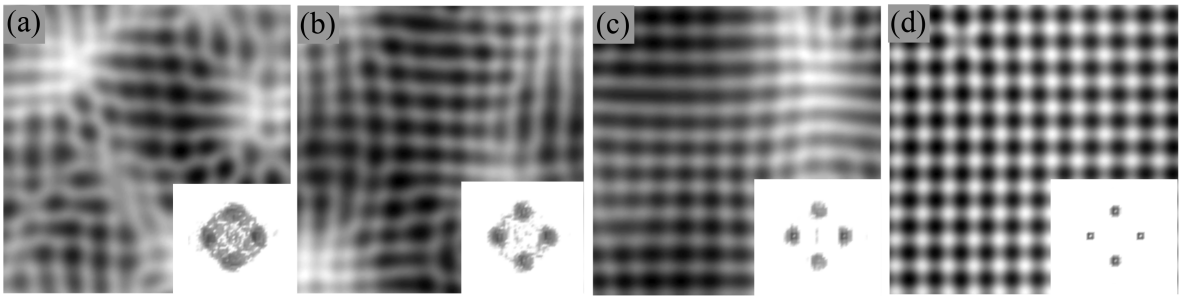

FIG. 6: Gray-scale plots of $u(x, y, t)$ at time $t = 30000$ with parameters $a = 0.25$ and $c = 1$ chosen from Region I. The remaining parameter values are $\rho = -0.5$, $b = 0.99b_T$, $\lambda = -1$, $\nu = 0$, $\eta = 10$, $\beta_1 = 0.25$, $\beta_2 = 0.25$, and (a) $\alpha_1 = \alpha_2 = 0.5$, (b) $\alpha_1 = \alpha_2 = 1$, (c) $\alpha_1 = \alpha_2 = 1.5$, (d) $\alpha_1 = \alpha_2 = 2$. The domain is $-60 \leq x, y \leq 60$. Insets show the Fourier transform on the domain $-10 \leq k_x, k_y \leq 10$.

and evolves into either patches of ripples aligned with the axes (Fig. 8) if $\gamma_1 < |\gamma_2|$ or a square pattern of ever-increasing length scale if $\gamma_1 > |\gamma_2|$ (Fig. 9). The pattern also coarsens in the case $\rho = 0$, as shown in Fig. 10.

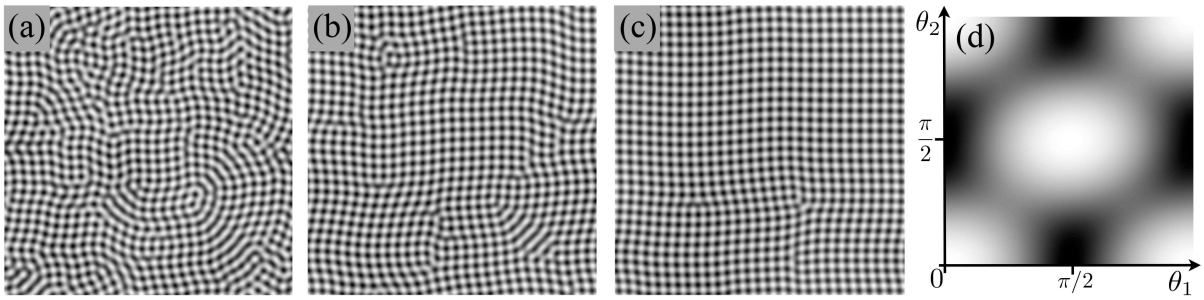

FIG. 7: (a)-(c) A time series of gray-scale plots of $u(x, y, t)$ with $a = 0.25$ and $c = 1$ chosen in Region I, and $\rho = 0$, $b = 0.96b_T$, $\lambda = 0$, $\nu = 0$, $\eta = 10$, $\alpha_1 = 1$, $\alpha_2 = 0$, $\beta_1 = 0.25$, and $\beta_2 = 0$. The times are (a) 1000, (b) 4000, (c) 18000, and the spatial domain is $-150 \leq x, y \leq 150$. The spatial grid for the simulation is 512×512. (d) A gray-scale plot of the effective potential (33) for the values of the parameters in the simulation of panels (a)-(c) as a function of θ_1 and θ_2. Darker shading indicates a lower value of the effective potential.

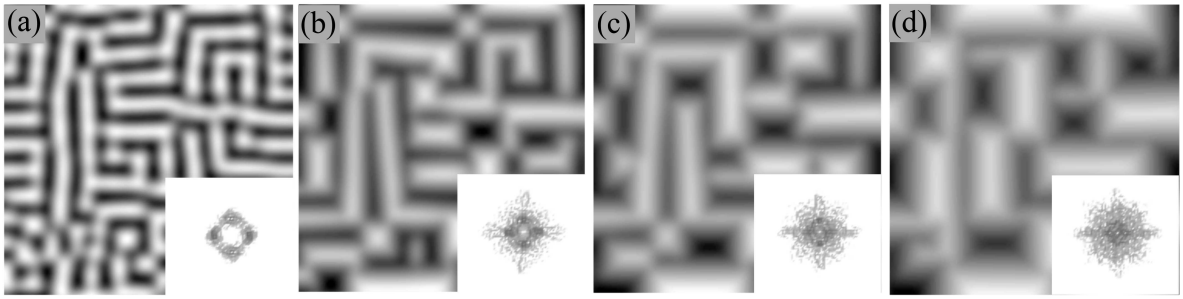

FIG. 8: A time series of gray-scale plots of $u(x, y, t)$ with parameters $a = 0.75$ and $c = 0.5$ chosen from Region II. The remaining parameter values are $\rho = -0.25$, $b = 0.94a$, $\lambda = 0$, $\nu = 0$, $\eta = 10$, $\alpha_1 = 0.25$, $\alpha_2 = 0$, $\beta_1 = 1$, and $\beta_2 = 0$. The times are (a) 4000, (b) 14000, (c) 30000, (d) 60000, (e) 80000, (f) 100000, and the domain is $-120 \leq x, y \leq 120$. Insets show the Fourier transform on the domain $-30 \leq k_x, k_y \leq 30$.

VI. CONCLUSIONS AND DISCUSSION

We have advanced a theory for the spontaneous pattern formation that occurs on the (001) surface of a crystalline binary material with fourfold rotational symmetry about the z axis when it is subjected to normal-incidence ion bombardment. The theory accounts for the Ehrlich-Schwoebel barrier which produces uphill atomic currents and results in cubic

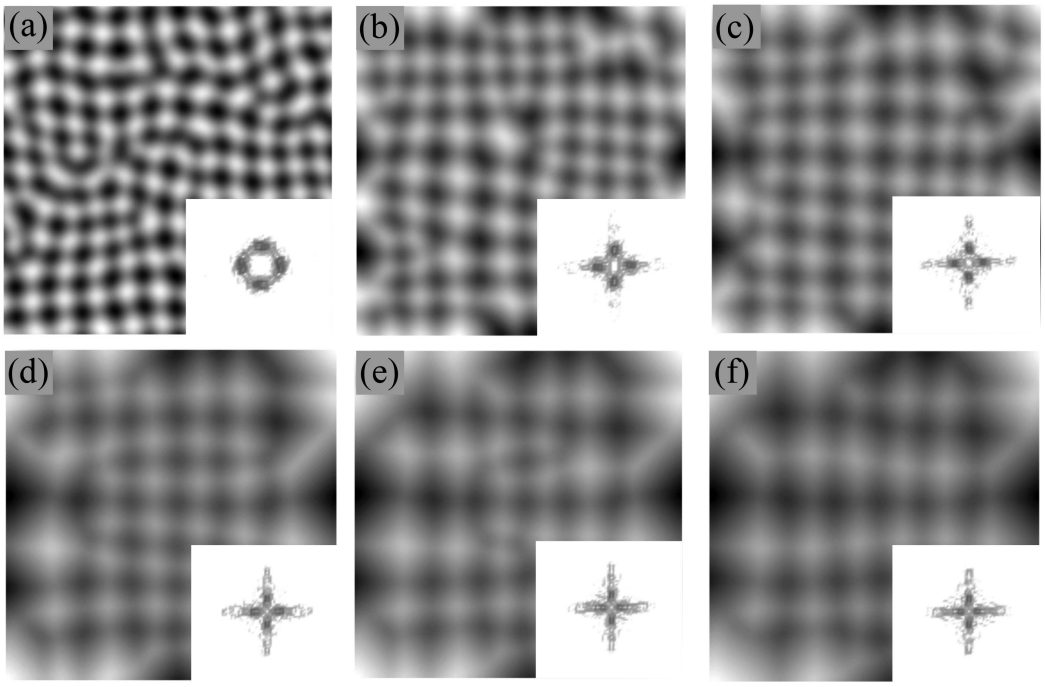

FIG. 9: A time series of gray-scale plots of $u(x, y, t)$ with parameters $a = 0.75$ and $c = 0.5$ chosen from Region II. The remaining parameter values are $\rho = -0.25$, $b = 0.94a$, $\lambda = 0$, $\nu = 0$, $\eta = 10$, $\alpha_1 = 1$, $\alpha_2 = 0$, $\beta_1 = 0.25$, and $\beta_2 = 0$. The times are (a) 4000, (b) 14000, (c) 30000, (d) 60000, (e) 80000, (f) 100000, and the domain is $-120 \leq x, y \leq 120$. Insets show the Fourier transform on the domain $-30 \leq k_x, k_y \leq 30$.

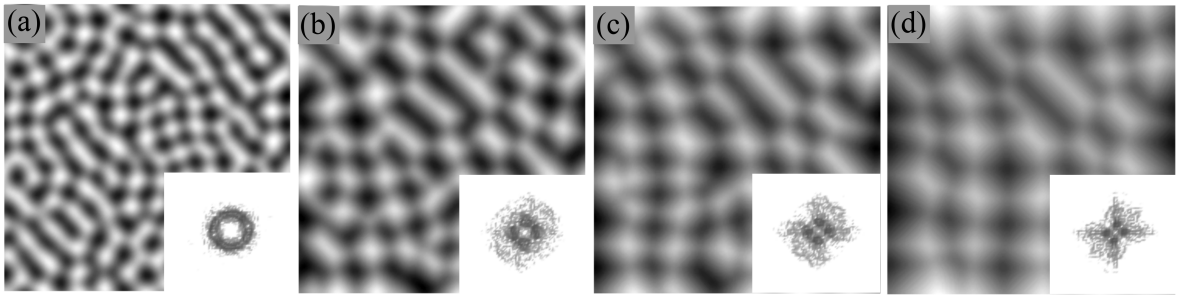

FIG. 10: A time series of gray-scale plots of $u(x, y, t)$ with parameters $a = 0.75$ and $c = 0.5$ chosen from Region II. The remaining parameter values are $\rho = 0$, $b = 0.94a$, $\lambda = 0$, $\nu = 0$, $\eta = 10$, $\alpha_1 = 1$, $\alpha_2 = 0$, $\beta_1 = 0.25$, and $\beta_2 = 0$. The times are (a) 4000, (b) 14000, (c) 30000, (d) 60000, (e) 80000, (f) 100000, and the domain is $-120 \leq x, y \leq 120$. Insets show the Fourier transform on the domain $-30 \leq k_x, k_y \leq 30$.

nonlinearities involving spatial derivatives of the field u, the deviation from a homogeneous surface height.

As for the case of irradiation of an amorphous binary material, the coupling between u and the surface composition ϕ is key to the formation of well-ordered patterns since it leads to a region of parameter space in which there is a narrow band of unstable wavelengths. Linear stability analysis shows that if the parameters a and c are chosen so that $a < c$ and $4a > (1-c)^2$ if $c < 1$, then there is a narrow band of unstable wavelengths. Weakly nonlinear analysis of the model in this region of parameter space and near the critical value of the bifurcation parameter b results in a system of ordinary differential equations for the amplitudes of the Fourier modes. Analysis of these amplitude equations predicts that if the coefficients of the cubic nonlinearities that describe the Ehrlich-Schwoebel barrier are large enough, and the coefficients of those terms obey certain relations (which roughly say that the coefficients α_1 and α_2 of the derivatives with respect to only one variable need to be sufficiently large compared to the coefficients β_1 and β_2 of the terms involving mixed derivatives), then highly ordered square arrays of nanopyramids can form. If the coefficients of the Ehrlich-Schwoebel barrier terms do not satisfy these conditions, then the analysis predicts the formation of well-ordered ripple patterns. These analytical results are supported by numerical simulations of the equations of motion. Histograms of the gradient of u have peaks at the four corners of a square for square array patterns and at either end of a pole for ripple patterns. The square arrays and ripple patterns produced in the presence of the Ehrlich-Schwoebel barrier therefore differ from those produced without this effect.

Cubic nonlinearities in the governing equations are essential for the formation of square arrays since these terms give rise to the cubic terms in the amplitude equations produced by the weakly nonlinear analysis. However, cubic nonlinearities of a very special form are needed for stable square patterns to develop [24]. The cubic nonlinearities that arise from an Ehrlich-Schwoebel barrier lead to solutions in which exactly four Fourier modes have nonzero amplitudes. For the square patterns to be stable, however, the coefficients γ_1 and γ_2 of the cubic nonlinearities in the amplitude equations must satisfy the condition $\gamma_1 > |\gamma_2|$. This condition is not satisfied by a simple cubic nonlinearity such as the term $\eta\phi^3$ that appears in the Bradley-Shipman theory.

Another key requirement for the formation of a well-ordered square array of nanopyramids is that the coefficients λ and ν of the quadratic terms in the governing equations

be sufficiently small. As we have shown in previous work, these terms are responsible for the formation of hexagonal arrays of nanodots in the case in which there is no Ehrlich-Schwoebel barrier [3–5]. Even if the conditions for a square pattern rather than a ripple pattern are satisfied, the quadratic terms can prevent the formation of well-ordered square arrays. For large enough values of the coefficients of the Ehrlich-Schwoebel barrier terms, however, well-ordered square arrays can occur even if the coefficients of the quadratic terms are nonzero.

The parameter ρ in our equations of motion is nonzero if the surface diffusion is anisotropic. For $\rho < 0$ and the bifurcation parameter b close to threshold, the wavevectors for which the real part of the linear growth rate, $\mathrm{Re}\,\sigma_+(\boldsymbol{k})$, is positive are confined to four small regions in wavevector space about each of the orthogonal pairs of wavevectors $\pm\boldsymbol{k}_1 = \pm(k_T, 0)$ and $\pm\boldsymbol{k}_2 = \pm(0, k_T)$. In this case, the square arrays are aligned with the coordinate axes. In contrast, if $\rho = 0$, there is an annulus of wavevectors in which $\mathrm{Re}\,\sigma_+(\boldsymbol{k}) > 0$, and so it not immediately apparent which pairs of wavevectors will be chosen by the dynamics. We obtained a prediction for the chosen wavevectors by finding the wavevectors that minimize the effective potential for the amplitude equations. This prediction is in accord with the results of our simulations. It has also been observed in other contexts, such as convection in a horizontal fluid layer [20] and phyllotactic pattern formation at plant meristems [21], that even for nongradient systems, the amplitude equations may be gradient near threshold and that solutions to the full system of PDEs coincide with minimizers of the effective potential for the amplitude equations.

In contrast to the case in which the parameters a and c are chosen from Region I, linear stability analysis shows that if a and c are chosen from Region II (that is, $a > c$), there is not a narrow band of unstable wavelengths. If $b < a$, then all wavelengths that exceed a critical value are unstable. Numerical explorations of this region in parameter space yield disordered ripple or square patterns that coarsen with time. The square patterns are similar to those produced in the experiments of Ou *et al.* [14] with an elemental crystalline target material. The equation of motion proposed by Ou *et al.* for the case of an elemental material also does not have a narrow band of unstable wavelengths. Although the amplitude equations derived in our weakly nonlinear analysis only apply if there is a narrow band of unstable wavelengths, our simulations suggest that the condition $\gamma_1 > |\gamma_2|$ may nonetheless serve as a guide to producing disordered square arrays if $a > c$.

Our theoretical results provide a strong motivation for experimental studies in which the (001) surfaces of the binary compound semiconductors PbSe, PbS, PbTe and SnTe are subjected to normal-incidence ion bombardment while being maintained at temperatures in excess of their respective recrystallization temperatures. These materials have fourfold rotational symmetry about the z axis. Our results establish that if the experimental parameters are appropriately chosen, highly ordered square arrays of nanoscale pyramids will develop. If successful, these experiments would yield a new entry in the short but growing list of well ordered nanopatterns that can be fabricated by bombardment of a solid surface with a broad ion beam.

Acknowledgments

One of us (R.M.B.) would like to thank Stefan Facsko, Leonardo Golubović and Xin Ou for valuable correspondence. R.M.B. and P.D.S. are grateful to the National Science Foundation for its support through grant DMR-1305449.

---

[1] V. B. Shenoy, W. L. Chan, and E. Chason, Phys. Rev. Lett. **98**, 256101 (2007).

[2] S. Facsko, T. Dekorsy, C. Koerdt, C. Trappe, H. Kurz, A. Vogt, and H. L. Hartnagel, Science **285**, 1551 (1999).

[3] R. M. Bradley and P. D. Shipman, Phys. Rev. Lett. **105**, 145501 (2010).

[4] P. D. Shipman and R. M. Bradley, Phys. Rev. B **84**, 085420 (2011).

[5] R. M. Bradley and P. D. Shipman, Appl. Surf. Sci. **258**, 4161 (2012).

[6] F. C. Motta, P. D. Shipman and R. M. Bradley, J. Phys. D (Fast Track Communications) **45**, 122001 (2012).

[7] F. C. Motta, P. D. Shipman, and R. M. Bradley, Phys. Rev. B **90**, 085428 (2014).

[8] S. A. Mollick, D. Ghose, P. D. Shipman and R. M. Bradley, Appl. Phys. Lett. **104**, 043103 (2014).

[9] U. Valbusa, C. Boragno and F. Buatier de Mongeot, J. Phys.: Condens. Matter **14** 8153 (2002).

[10] A. Levandovsky and L. Golubović, Phys. Rev. B **69**, 241402 (2004).

[11] E. Chason and W. L. Chan, Topics Appl. Physics **116**, 53 (2010).

[12] L. Golubović, A. Levandovsky and D. Moldovan, E. Asian J. Appl. Math. **1**, 297 (2011).

[13] G. Costantini, F. Buatier de Mongeot, C. Boragno, and U. Valbusa, Phys. Rev. Lett. **86**, 838 (2001).

[14] X. Ou, A. Keller, M. Helm, J. Fassbender, and S. Facsko, Phys. Rev. Lett. **111**, 016101 (2013).

[15] X. Ou, K.-H. Heinig, R. Hübner, J. Grenzer, X. Wang, M. Helm, J. Fassbender and S. Facsko, Nanoscale **7**, 18928 (2015).

[16] The same transformation was used in a study of the bombardment of an amorphous elemental target by four identical ion beams whose azimuthal angles differ by 90° increments. See S. Vogel and S. J. Linz, Phys. Rev. B **75**, 085425 (2007).

[17] R. Hoyle, *Pattern Formation: An Introduction to Methods* (Cambridge University Press, Cambridge, England, 2007).

[18] M. Cross and H. Greenside, *Pattern Formation and Dynamics in Nonequilibrium Systems*, (Cambridge University Press, Cambridge, England, 2009).

[19] D. Walgraef, *Spatio-Temporal Pattern Formation* (Springer, New York, 1996).

[20] F. H. Busse, J. Math. Phys. **46**, 140 (1967).

[21] M. Pennybacker, P. D. Shipman, A. C. Newell, Physica D **306**, 48-81 (2015).

[22] S. M. Cox and P. C. Matthews, J. Comp. Phys. **176**, 430 (2002).

[23] R. V. Craster and R. Sassi, Tech. Report No. 99, Università degli studi di Milano (2006).

[24] W. Pesch and L. Kramer, Z. Phys. B–Condensed Matter **63**, 121 (1986).